

An Improved Evaluation of the Neutron Background in the PandaX-II Experiment

QiuHong Wang^{*1,13}, Abdusalam Abdukerim², Wei Chen², Xun Chen², Yunhua Chen³, Xiangyi Cui², Yingjie Fan⁴, Deqing Fang¹, Changbo Fu², Lisheng Geng⁵, Karl Giboni², Franco Giuliani², Linhui Gu², Xuyuan Guo³, Ke Han², Changda He², Di Huang², Yan Huang³, Yanlin Huang⁶, Zhou Huang², Peng Ji⁴, Xiangdong Ji^{2,7}, Yonglin Ju⁸, Yihui Lai², Kun Liang², Huaxuan Liu⁸, Jianglai Liu^{†2,7}, Wenbo Ma², Yugang Ma¹, Yajun Mao⁹, Yue Meng², Parinya Namwongsa², Kaixiang Ni², Jinhua Ning³, Xuyang Ning², Xiangxiang Ren^{8,2}, Changsong Shang³, Lin Si², Andi Tan¹⁰, Anqing Wang¹¹, Hongwei Wang¹, Meng Wang¹¹, Siguang Wang⁹, Xiuli Wang⁸, Zhou Wang^{10,12,2}, Mengmeng Wu⁴, Shiyong Wu³, Jingkai Xia², Mengjiao Xiao^{10,12}, Pengwei Xie⁷, Binbin Yan¹¹, Jijun Yang², Yong Yang², Chunxu Yu⁴, Jumin Yuan¹¹, Dan Zhang¹⁰, Hongguang Zhang², Tao Zhang², Li Zhao², Qibin Zheng⁶, Jifang Zhou³, Ning Zhou², and Xiaopeng Zhou⁵

(PandaX-II Collaboration);

¹Shanghai Institute of Applied Physics, Chinese Academy of Sciences, Shanghai 201800, China;

²INPAC and School of Physics and Astronomy, Shanghai Jiao Tong University,

Shanghai Laboratory for Particle Physics and Cosmology, Shanghai 200240, China;

³Yalong River Hydropower Development Company, Ltd., 288 Shuanglin Road, Chengdu 610051, China;

⁴School of Physics, Nankai University, Tianjin 300071, China;

⁵School of Physics & International Research Center for Nuclei and Particles in the Cosmos & Beijing Key Laboratory of Advanced Nuclear Materials and Physics, Beihang University, Beijing 100191, China;

⁶School of Medical Instrument and Food Engineering, University of Shanghai for Science and Technology, Shanghai 200093, China;

⁷Tsung-Dao Lee Institute, Shanghai 200240, China;

⁸School of Mechanical Engineering, Shanghai Jiao Tong University, Shanghai 200240, China;

⁹School of Physics, Peking University, Beijing 100871, China;

¹⁰Department of Physics, University of Maryland, College Park, Maryland 20742, USA;

¹¹School of Physics and Key Laboratory of Particle Physics and Particle Irradiation (MOE), Shandong University, Jinan 250100, China;

¹²Center of High Energy Physics, Peking University, Beijing 100871, China;

¹³University of Chinese Academy of Sciences, Beijing 100049, China

In dark matter direct detection experiments, neutron is a serious source of background, which can mimic the dark matter-nucleus scattering signals. In this paper, we present an improved evaluation of the neutron background in the PandaX-II dark matter experiment by a novel approach. Instead of fully relying on the Monte Carlo simulation, the overall neutron background is determined from the neutron-induced high energy signals in the data. In addition, the probability of producing a dark-matter-like background per neutron is evaluated with a complete Monte Carlo generator, where the correlated emission of neutron(s) and γ (s) in the (α, n) reactions and spontaneous fissions is taken into consideration. With this method, the neutron backgrounds in the Run 9 (26-ton-day) and Run 10 (28-ton-day) data sets of PandaX-II are estimated to be 0.66 ± 0.24 and 0.47 ± 0.25 events, respectively.

dark matter, direct detection, xenon, neutron background, high energy gamma, neutron generator

PACS number(s): 95.35.+d, 29.40.n, 28.20.v

*Corresponding author: wangqiuHong@sinap.ac.cn

†Spokesperson: jianglai.liu@sjtu.edu.cn

1 Introduction

Modern astronomical and cosmological observations have firmly established the existence of dark matter (DM) in our Galaxy and the Universe [1]. Since the seminal paper by Goodman and Witten [2], there has been an intensive global effort of DM direct detection, searching for the nuclear recoil (NR) of the atomic nucleus in the target induced by galactic DM particles.

As one of such experiments, the PandaX experiment, located at the China Jinping Underground Laboratory [3] uses liquid xenon as the DM direct detection target [4]. The second phase of this experiment, PandaX-II [5], contains a total of 1.1 tons of liquid xenon in a stainless steel (SS) cryostat with low levels of radioactivity [6]. Approximately 580 kg of liquid xenon is confined inside the 60-cm high and 60-cm diametral dual phase xenon time projection chamber (TPC) with Hamamatsu R11410 photomultipliers (PMTs) located at the top and bottom. For each recoil event, the prompt scintillation photons ($S1$) and the delayed electroluminescence photons ($S2$) from ionized electrons can be detected by those two arrays of PMTs. Highly reflective polytetrafluoroethylene (PTFE) layers are installed surrounding the TPC to enhance the photon collection efficiency. So far, PandaX-II has released two data sets, the Run 9 (79.6 live days, 26-ton-day exposure) [5] and Run 10 (77.1 live days, 28-ton-day exposure) [7].

From the background point of view, the charge ratio of $S2$ to $S1$ offers a strong discriminant for the NR signals against the electron recoil (ER) background events from γ s and β s. On the other hand, the neutrons could produce single-site scattering NR (SSNR) events that highly resemble the DM interactions. External neutrons can be reduced to a negligible level via carefully designed shielding. However, neutrons can be produced internally from radioactivities in the detector materials through two main reactions, the (α, n) reaction and spontaneous fission (SF) of ^{238}U , and bring about a non-negligible background to the DM detection.

Traditionally, neutron background evaluation is heavily simulation-based. In this paper, we present a novel data-driven method to evaluate the neutron background in PandaX-II, utilizing neutron-induced high energy gamma (HEG) events as the normalization. The rest of this paper is organized as follows. In sect. 2, we explain our improved method of the SSNR background evaluation. In sect. 3, we use the ^{241}Am - ^9Be (AmBe) neutron calibration data to understand the SSNR and HEG events. In sect. 4, we discuss our improved neutron generator model and establish an expected ratio between the two types of events originating from the detector materials. A new estimation of the neutron background

level in PandaX-II is given in sect. 5, followed by a summary in sect. 6.

2 Method

Traditionally, the SSNR background estimation for DM experiments has the following three ingredients, 1) radioactivities of detector materials, 2) a model which converts the radioactivities to the number of neutrons produced and their energy spectrum, and 3) a detector Monte Carlo (MC) simulation which uses the model as the event generator and carries out detailed simulation of neutron interactions and the detector response. The SSNR background is calculated as

$$\begin{aligned} N_{\text{ssnr}} &= \sum_{ij} P_{\text{ssnr},ij} \times n_{ij} \times T \\ n_{ij} &= Y_{ij} \times A_{ij} \times M_i. \end{aligned} \quad (1)$$

In these expressions, n_{ij} is the neutron production rate from a detector component i due to a given radionuclide or a reaction chain j , calculated by combining the radioactivity per unit mass A_{ij} , the neutron yield Y_{ij} , and the component mass M_i . Y_{ij} is typically computed by the SOURCES-4A code [8], which calculates the (α, n) and SF neutron production rates and spectra using evaluated libraries. $P_{\text{ssnr},ij}$ is the probability of producing an SSNR signal per neutron calculated by the detector MC and T is the duration of the measurement.

The above method has two serious drawbacks. First, SOURCES-4A and the resulting neutron generator treat every neutron as an isolated particle. This is, in fact, a biased assumption - there is a high probability that the neutron(s) is generated in association with γ (s) in the (α, n) and SF reactions, leading to multi-site scatterings and mixed ER-NR energy depositions. Second, the uncertainty in radioassay of detector materials A_{ij} would be directly translated into a normalization uncertainty in the SSNR rate, which lacks experimental handle.

In light of the above, we developed a new method to estimate the neutron background. A complete neutron generator was developed which incorporates the correlated emission of neutron(s) and γ (s). This allows us to establish a more robust relationship between the SSNR events and the neutron-induced HEG events. Then the SSNR background can be estimated as

$$N_{\text{ssnr}} = N_{\text{heg}} \times R_{\text{mc}} = N_{\text{heg}} \times \left(\frac{\sum_{ij} P_{\text{ssnr},ij} \times n_{ij}}{\sum_{ij} P_{\text{heg},ij} \times n_{ij}} \right) \quad (2)$$

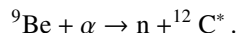
where N_{heg} is the number of identified HEG events from DM data, which serves as an *in situ* normalization. R_{mc} is an MC-based ratio between the summed SSNR and HEG events from individual components, obtained by folding the neutron

production rate n_{ij} and the probability to produce an SSNR (HEG) event, $P_{\text{ssnr},ij}$ ($P_{\text{heg},ij}$). In what follows, we shall first use the AmBe calibration to understand the connection between SSNR and HEG events, then discuss our evaluation of R_{mc} and N_{heg} in turn.

3 The AmBe calibration

3.1 The AmBe neutron source

Two AmBe sources with the identical design were fabricated by the Atomic High Technology Co., Ltd. [9]. The sources produce neutrons via the (α, n) reaction



Two channels, (α, n_0) and (α, n_1) , dominate the reaction, in which ${}^{12}\text{C}^*$ is produced in the ground and the first excited state, respectively. The latter channel emits a single de-excitation γ ray of 4.4 MeV together with the neutron. The neutron energy spectra of the two channels can be calculated by combining a stand-alone Geant4-based [10, 11] simulation (energy loss process of α) and the JENDL database [12] (neutron production) and are shown in Figure 1. One of the two AmBe sources was deployed into the Daya Bay detector, where the simulated energy spectra were validated through measurement [13]. The other one was used for the calibration of PandaX-II.

The AmBe source was deployed inside two separate horizontal PTFE tubes encircling the cryostat, at a vertical height of 1/4 (lower) and 3/4 (upper) of the TPC. The AmBe calibration runs in PandaX-II were performed more than 20 times, interspersed among the DM data taking, with the source located at different locations in the loops. In total,

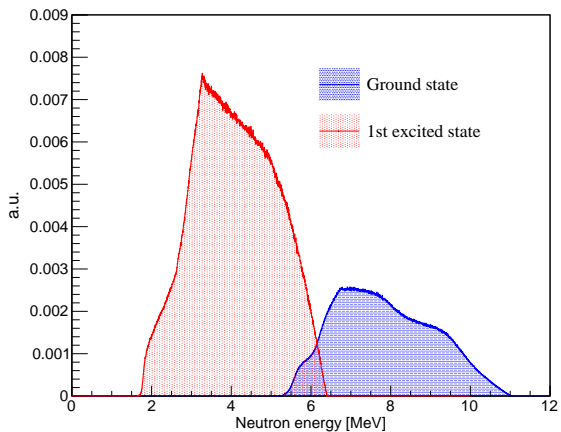


Figure 1 The neutron energy spectrum of the AmBe source from simulation, with the two histograms corresponding to (α, n_0) (red) and (α, n_1) (blue).

6.8 and 22.8 days of AmBe data were taken in Run 9 and Run 10, respectively, with a source-induced rate of approximately 2 Hz. For different source locations, no significant difference was identified in the data or the MC, so we made no distinction in the calibration data analysis.

3.2 AmBe data

AmBe neutrons can produce the SSNR signal through elastic neutron-xenon-nucleus scattering if the scattering happens to be single-site in the TPC. More often, however, AmBe neutrons would scatter with xenon nuclei inelastically, producing NR signals mixed with ER signals from the nuclear de-excitation. In both cases above, the energy deposition is “prompt”, and may be further mixed with the “prompt” ER signals produced by the 4.4 MeV γ ray. On the other hand, after being thermalized, neutrons are also likely to be captured by xenon nuclei, which produces “delayed” high energy γ rays with a few μs delay time. These neutron-induced HEGs, regardless if produced promptly or by delayed capture, are related to the SSNR events through the parent neutrons.

In the AmBe calibration data sets, SSNR events are selected using identical cuts for dark matter data selection [5, 7], with $S1$ from 3 to 45 photoelectrons (PE) and $S2$ from 100 PE (raw) to 10000 PE (corrected for position uniformity). These cuts correspond to an electron-equivalent energy range between 1 and 10 keV $_{ee}$ approximately. The same fiducial volume (FV) cuts in Run 9 and Run 10 are adopted here.

The HEGs are easy to be identified because their total energy can be significantly higher than those from natural radioactivities. In addition, γ s can be produced at different times (prompt or delayed) and tend to have multiple scatterings with xenon, resulting in multiple $S1$ s and $S2$ s. A small fraction of them contain a separated NR signal before the HEGs from the delayed capture. An example of such waveforms is shown in Figure 2.

In the HEG event selection, the data quality cuts developed in Ref. [14] are inherited for each $S1$ and $S2$. For each scattering, the horizontal position is reconstructed using the

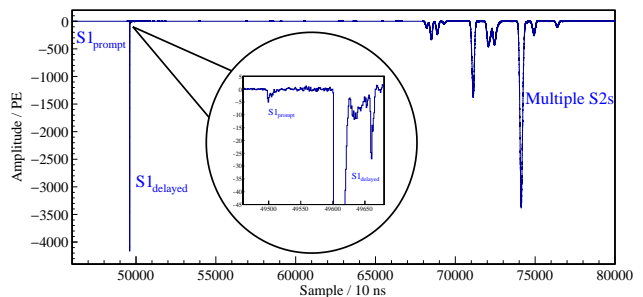


Figure 2 An example of waveforms of high energy neutron capture events in AmBe runs, in which the prompt NR occurred before the delayed HEGs.

so-called PAF reconstruction [5]. The approximate vertical positions of the scatterings are estimated by pairing these $S2$ s with the maximum $S1$ ¹⁾. Since we are interested in the HEGs with energies larger than 5.0 MeV (Q value of ^{208}Tl , the maximum ER energy by natural radioactivity), there is no need of a restrictive FV cut for background rejection. We select all $S2$ s within an extended FV (EFV) with a loose radius-square cut of $r^2 < 1000 \text{ cm}^2$ and a vertical position cut of 1.7 and 3.3 cm away from the cathode and gate, respectively, resulting in a target xenon mass of 502 kg. The total energy is computed by combining all $S1$ s and $S2$ s within the EFV²⁾. To avoid saturation of the PMTs at this high energy, the $S2$ signals in the bottom PMT array ($S2_b$), scaled by a factor of 3.5, are used in the reconstruction. A corrected energy, E_{corr} , is obtained by further applying a polynomial correction to align the energy of the identified γ events, i.e. 609 keV (^{214}Bi), 911/934 keV ($^{228}\text{Ac}/^{214}\text{Bi}$), 1173 keV (^{60}Co), 1332 keV (^{60}Co), 2614 keV (^{208}Tl), 4439 keV ($^{12}\text{C}^*$), 6467 keV ($^{132}\text{Xe}^*$) and 9255 keV ($^{130}\text{Xe}^*$), to their expected values.

The event distributions in $\log_{10}(\sum S2_b / \sum S1)$ vs. E_{corr} for the Run 9 and Run 10 AmBe data are shown in Figure 3. HEGs are selected within a 3σ cut on the high energy ER band, and with $E_{\text{corr}} > 6.2 \text{ MeV}$, about 3σ away from 5 MeV, as indicated in Figure 3. Some events are observed with lower vertical values than the main ER band. They are all α -related events, resulting in smaller ionization signals ($S2$ s). We categorize the events into three classes according to the vertical values from high to low, i.e., the mixed α -ER-events from the internal radon background, the bulk α s, and the wall α s whose ionization signals cannot be efficiently extracted. The α -ER-mixed events have a rate much lower than the AmBe-induced HEG rate here and therefore can be safely omitted.

The number of selected HEG and SSNR events and their ratios are summarized in Table 1, as compared with the simulation to be described in sect. 3.3.

3.3 AmBe simulation

A custom Geant4-based program (BambooMC), with the full PandaX-II geometry implemented, is used to simulate energy depositions in the detector by the radiation from the AmBe source. An event generator that samples the neutron energy from Figure 1, with correlated emission of 4.4 MeV γ ray for the (α, n_1) channel, is used to create primary particles. Note that the correlated γ emission in this generator is implemented by hand, effectively equivalent to the improved (α, n) generator discussed later in sect. 4.2. For SSNR events, the energy depositions are converted to simulated $S1$ and $S2$

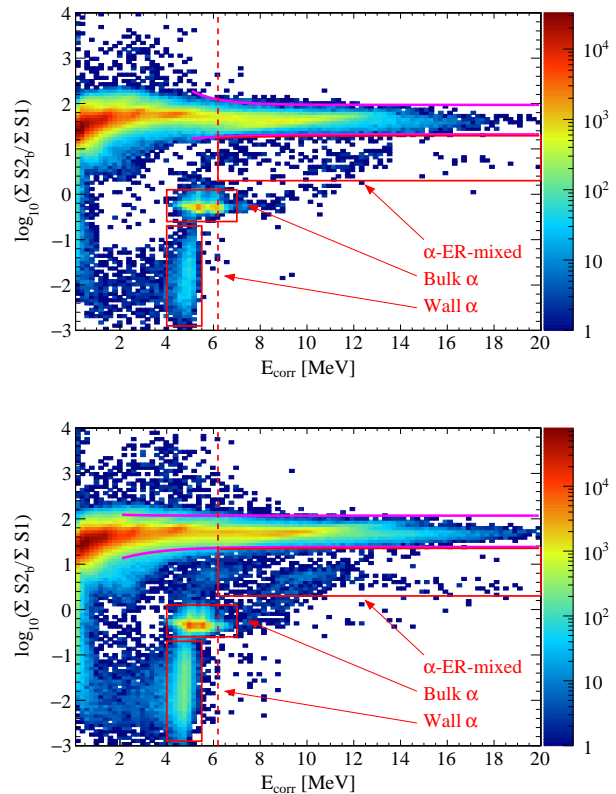


Figure 3 The distributions of events in $\log_{10}(\sum S2_b / \sum S1)$ vs. E_{corr} in the Run 9 (top) and Run 10 (bottom) AmBe data. The $\pm 3\sigma$ cuts of the ER band are shown as the solid magenta lines. The dashed red lines represent the 6.2 MeV cut for the HEGs. Also indicated below the ER band are the α -ER-mixed, bulk α s, and wall α events near the PTFE reflectors.

Table 1 The number of SSNR, HEG events and their ratios in Run 9 and Run 10 AmBe calibration data. The corresponding ratios from the simulation are also listed.

AmBe Run	Data			MC
	# SSNR	# HEG	Ratio	Ratio
Run 9	3415	49159	1/14.4	1/14.7
Run 10	10390	151783	1/14.6	1/15.2

signals using a NEST-based model [15]. For HEG events, instead of running the NEST-based simulation to produce $S1$ s and $S2$ s, we simply sum the true energy depositions within the EFV, and make a gentle energy-dependent Gaussian smearing with a σ varying from 4% to 10% from 1 MeV to 10 MeV, to best match the measured HEG spectrum from the AmBe data. The efficiencies of event detection and selection cuts from AmBe data are also incorporated into the MC simulation for the SSNR and HEG events.

The MC simulation is validated in several ways. In Fig-

1) Since neutron capture in xenon happens within a few μs (Figure 5), it is reasonable to simply use $S1_{\text{max}}$ as the T_0 of the drift.

2) Note that in the data, the contributions to $S1$ from the energy depositions inside or outside the EFV cannot be separated. This leads to a slight discrepancy in the energy reconstruction in the data and MC, however its impact is constrained by the spectra comparison in Figure 4

ure 4, the spectra of the measured (non-AmBe background subtracted) and simulated E_{corr} are overlaid, where the simulation is normalized to the data between 2 and 20 MeV. The spectra agree with each other well. A residual difference between Runs 9 and 10 is observed, which is likely from the difference in the PMT saturation because of the varying supply voltages [7]. The fractional difference (data–MC) of the HEGs between 6.2 to 20 MeV is 16.3% for Run 9 and 18.3% for Run 10, indicating the level of systematic uncertainties.

To validate the neutron capture process in the MC, we compare the time separation between the prompt and delayed energy deposition in the data and MC. Many neutron events in the data do not have a prompt $S1$ because the prompt energy is deposited in the dead region. To cleanly select events with a genuine prompt $S1$, we make a cut at 40 keV in both the data and MC. This energy corresponds to the de-excitation γ of ^{129}Xe excited by the neutron. Then we look for the second $S1$ corresponding to the delayed capture and obtain the distribution of the time difference. A comparison between the data and MC is shown in Figure 5, where one observes a fairly good agreement above $1 \mu\text{s}$. The discrepancy below $1 \mu\text{s}$ is likely due to the inefficiency in identifying two $S1$ s from the data when they are close-by. On the other hand, the selection of HEGs from the data does not require prompt-delayed $S1$ pairs, therefore is entirely unaffected.

Lastly, to quantify the global agreement between the AmBe data and MC, we compare the ratios between SSNR and HEG events in Table 1. For both run periods, the data and MC ratios are consistent within 4%. An increased number of SSNR events by a factor of 20% is obtained by an MC simulation without the 4.4 MeV γ in the source generator. The difference would further increase when the isolated neutrons

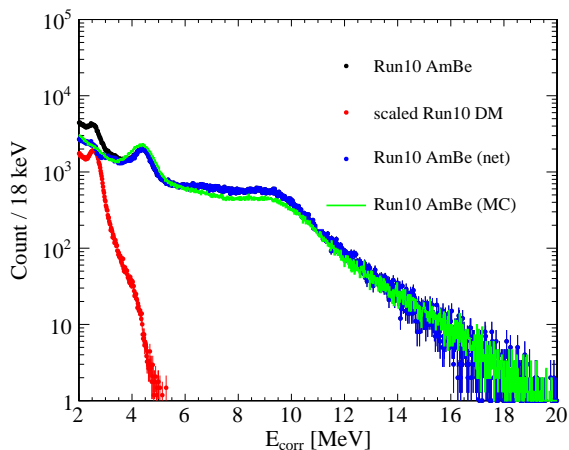


Figure 4 The raw AmBe (black), background (red), and net AmBe (blue) energy spectra in Run 10. The background spectrum is obtained from the DM data, scaled by the run durations. The net AmBe spectrum is obtained by subtracting the background from the raw AmBe spectrum. The simulated energy spectrum is overlaid in green.

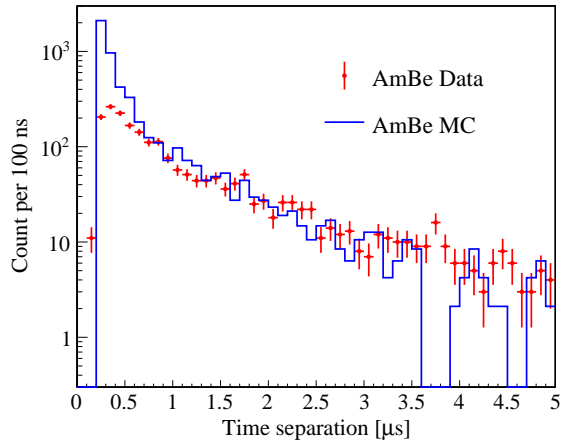


Figure 5 The time separation between the 40 keV prompt γ rays from $^{129}\text{Xe}^*$ and the delayed HEGs from neutron capture in Run 10 AmBe data (red) and MC (blue).

are produced at the PTFE or PMTs closer to the xenon target. This demonstrates the importance of correlated γ emission in the neutron production model.

4 The improved simulation

In this section, we developed an improved MC to calculate the ratio between SSNR and HEG events induced by radiogenic neutrons (R_{mc} in Eqn. 2) in the DM data.

4.1 Evaluation of neutron production rate

^{238}U , ^{235}U , and ^{232}Th decay chains are long-lived α emitters. Due to the low Coulomb potential, (α, n) events are mostly produced on the light nuclei in the detector, such as fluorine in the PTFE reflector wall, aluminum in the ceramic stem of the PMTs, silicon in the quartz window of the PMTs, etc. In addition, those decay chains also produce SF neutrons. As the input to the simulation, the radioactivities of the most important components for neutron production in the detector are summarized in Table 2.

The neutron yields, Y_{ij} , are calculated with SOURCES-4A and summarized in Table 3. The SF neutron yield of $^{238}\text{U}_e$ is 1.1×10^{-6} neutrons/decay, and that of other chains are negligible. The neutron production rate by each component, $\sum_j n_{ij}$, by combining the radioactivities and neutron yields, is also listed in the table, where dominating contribution from PTFE can be observed. The typical contribution to neutron production from SF is about 4% of that from (α, n) .

4.2 New (α, n) generators

In recent years, improved low energy nuclear models and data libraries have been incorporated into Geant4 [18]. Therefore,

Table 2 The activities of the materials used for neutron background estimation in the PandaX-II experiment. For ^{238}U , its early chain ($^{238}\text{U}_e$) represents $^{238}\text{U} \rightarrow ^{230}\text{Th}$, and the later chain ($^{238}\text{U}_l$) refers to $^{226}\text{Ra} \rightarrow ^{206}\text{Pb}$. For ^{232}Th , the early chain ($^{232}\text{Th}_e$) and later chain ($^{232}\text{Th}_l$) refer to $^{232}\text{Th} \rightarrow ^{228}\text{Ac}$ and $^{228}\text{Th} \rightarrow ^{208}\text{Pb}$, respectively. The activities of the SS and PTFE were measured with the PandaX counting station [16] assuming secular equilibrium. The radioactivities from the 3-in PMTs are taken from Ref. [17].

Component (Material)	Quantity	Radioactivity (mBq/kg or mBq/piece)				
		$^{238}\text{U}_e$	$^{238}\text{U}_l$	^{235}U	$^{232}\text{Th}_e$	$^{232}\text{Th}_l$
PTFE	55.5 kg	3.2	3.2	1.3	1.5	1.5
Cryostat (SS)	256.9 kg	1.7	1.7	2.4	2.7	2.7
PMT stem (Al_2O_3)	110 piece	2.4	0.3	0.1	0.2	0.1
PMT window (SiO_2)	110 piece	1.2	0.07	0.02	0.03	0.03

Table 3 Neutron yields of ^{238}U , ^{235}U , and ^{232}Th in different materials. Among all channels, fluorine has the largest (α, n) neutron yield. SF only happens in the earl chain, with a yield of about 2 orders less compared to the (α, n). The neutron production rates, $\sum_j n_{ij}$, are also listed for corresponding component i .

Material	Neutron yield (neutrons/decay)					$\sum_j n_{ij}$ (neutrons/day)
	$^{238}\text{U}_e$	$^{238}\text{U}_l$	^{235}U	$^{232}\text{Th}_e$	$^{232}\text{Th}_l$	
PTFE	7.6×10^{-6}	5.5×10^{-5}	8.9×10^{-5}	7.9×10^{-7}	8.6×10^{-5}	2.1×10^0
SS	1.1×10^{-6}	4.1×10^{-7}	3.4×10^{-7}	4.9×10^{-11}	1.5×10^{-6}	1.7×10^{-1}
Al_2O_3	1.3×10^{-6}	6.3×10^{-6}	9.5×10^{-6}	1.3×10^{-8}	1.1×10^{-5}	6.6×10^{-2}
SiO_2	1.2×10^{-6}	9.9×10^{-7}	1.5×10^{-6}	7.8×10^{-9}	1.6×10^{-6}	1.5×10^{-2}

as a remedy to SOURCES-4A, we utilized Geant4 (version 10.03p03) and developed a new (α, n) neutron generator to include the excitation/de-excitation of the outgoing nucleus.

In Geant4, the *INCL++* model handles the nuclear reactions and *G4ExcitationHandler* models the nuclear excitations/de-excitations [18]. Long-lived decay chains are launched automatically by Geant4, and for events where the neutron is produced via (α, n), the information of the energy and particle IDs of the production vertices are stored. It is identified that in the native *G4ExcitationHandler*, the first γ in a cascade disrespects the known energy level in the final nucleus. This causes a significant and incorrect suppression for the (α, n_0) channel relative to the others. A fix is implemented to correct the inappropriate γ energy and absorb the difference to the kinetic energy of the neutron [19]. The corrected kinetic energy of the neutron and different γ energies (if any) are then stored and later used as the primary generator of BambooMC. For simplicity, the directions of neutron and γ (s) are assumed to be isotropic.

We carried out a BambooMC simulation with the improved generator for ^{238}U in PTFE. The results are summarized in Table 4, together with that by the SOURCES-4A generator. Clearly, the former leads to a suppression in the SSNR events by a factor of four due to the correlated γ emission, consistent with the expectation in sect. 3.3.

Table 4 The P_{ssnr} , P_{heg} , and their ratio predicted for ^{238}U in PTFE by the two (α, n) generators. 10^6 events are generated in both simulations. See text for details.

Generator	P_{ssnr}	P_{heg}	Ratio
Improved	1038/10 ⁶	27602/10 ⁶	1/26.6
SOURCES-4A	3997/10 ⁶	26171/10 ⁶	1/6.5

4.3 New SF generator

Similar to the (α, n) reaction, multiple neutrons and γ s are produced in the SF of ^{238}U . The average neutron and γ multiplicities are 2.0 and 6.4, respectively [20], which was not taken into account in the SOURCES-4A generator. Following the practice in Ref. [21], we employed a special Geant4-based program to simulate the SF of ^{238}U . This program incorporates the LLNL Fission Library 2.0.2 including a special FREYA model [22] that takes into account the correlations in neutron multiplicity, energy, angles, and the energy sharing between neutrons and γ s. Using this new generator with BambooMC, we generated SF of ^{238}U in the PTFE materials, and the resulting SSNR and HEG events are shown in Table 5. Also shown in the same table are those using the SOURCES-4A generator. Due to the large neutron and γ multiplicity, the SSNR events are suppressed to a negligible level in comparison to the (α, n) reaction.

4.4 Evaluation of R_{mc}

We performed BambooMC simulation for all detector materials in Table 2 with the improved neutron generators. The

Table 5 The P_{ssnr} , P_{heg} , and their ratio predicted for ^{238}U in PTFE by the two SF generators. 10^6 events are generated in both simulations. “2.0” is the mean number of neutrons per fission. See text for details.

Generator	P_{ssnr}	P_{heg}	Ratio
Improved	89/2.0/10 ⁶	86693/2.0/10 ⁶	1/974.1
SOURCES-4A	3885/10 ⁶	27771/10 ⁶	1/7.1

same cuts used in the analysis of AmBe MC were used to select the SSNR and HEG events. The results are shown in

Table 6. Due to the high neutron yield and the high ^{238}U impurity level, the contribution from PTFE dominates the SSNR and HEG events. The naively estimated SSNR background according to Eqn. 1 is about 0.2 events for both Run 9 and Run 10, respectively. As we have mentioned in sect. 2, these values heavily rely on the input of the radioactivities, therefore lack robustness. The overall ratios between the SSNR and HEG events are 1/26.6 for Run 9 and 1/24.6 for Run 10. The difference mainly arises from different FV for SSNR selections in Run 9 and Run 10 [7] (due to different levels of ^{127}Xe background). The uncertainties of R_{mc} are estimated to be 16.3% and 18.3% for Run 9 and Run 10, respectively, based on the spectra difference of HEG events in AmBe data and MC, discussed in sect. 3.3.

5 Improved neutron background estimation in PandaX-II

As discussed in Secs. 3.2 and 3.3, neutrons can induce HEG events in xenon target, with a rate much higher than the SSNR events. Therefore in PandaX-II DM data, we look for HEGs and estimate the corresponding SSNR background from detector materials using the R_{mc} in sect. 4.4.

We selected HEGs from the DM data using the same procedures as those in analyzing the AmBe data. At the high energy region of a few MeVs, the distributions of $\log_{10}(\sum S2_b / \sum S1)$ vs. E_{corr} in Run 9 and Run 10 DM data are shown in Figure 6. The fact that the PMTs in Run 9 and Run 10 were operated at different high voltage [7] leads to different saturation for large $S1$ s and $S2$ s, thereby some difference in the high energy event distributions. 36 and 20 HEG candidates are found in Run 9 and Run 10, respectively. However, different from the AmBe data, due to the much lower rate of HEGs, the α -ER-mixed events become more pronounced and can contaminate the true HEGs.

Since an α cannot scatter twice in the detector, one expects that the α -mixed events contain less amount of $S2$ s than the γ cascade in the HEGs. This is confirmed further in Figure 7, where the distributions of the number of $S2$ s vs. E_{corr} for HEGs in AmBe data and the α -mixed events below the ER band in DM data (as indicated in Figure 6) are compared. An α -rejection cut is developed (green curve in Figure 7), with an 82% (61%) efficiency on HEGs for Run 9 (Run 10) estimated from AmBe data, with an estimated systematic uncertainty of 10.5%. The corresponding rejection power for α -mixed events are $91\pm 1\%$ and $89\pm 1\%$, respectively, estimated from DM data.

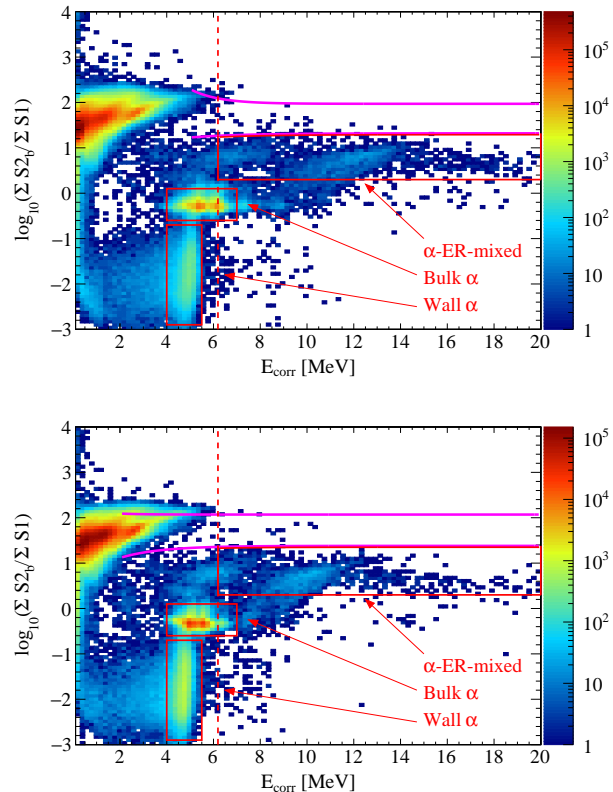


Figure 6 The distributions of events in $\log_{10}(\sum S2_b / \sum S1)$ vs. E_{corr} in the Run 9 (top) and Run 10 (bottom) DM data.

After applying the α -rejection cut, the band distributions of the surviving events in Run 9 and Run 10 DM data are shown in Figure 8. In total, 16 and 8 HEG candidates survive in Run 9 and Run 10, respectively. The final HEG candidates have multiple $S2$ s, consistent with those from the AmBe data, with an example waveform shown in Figure 9. The residual α -mixed background is estimated to be 1.7 ± 0.7 and 0.9 ± 0.7 events based on the cut efficiency and rejection power mentioned above. The background subtracted and efficiency corrected HEGs, N_{heg} , are 17.5 ± 5.6 events in Run 9 and 11.6 ± 5.7 events in Run 10, where the statistical and systematic uncertainties are combined.

Using N_{heg} obtained from the data and Eqn. 2, the improved estimation of SSNR background is now 0.66 ± 0.24 and 0.47 ± 0.25 events for Run 9 and Run 10, respectively, in which the uncertainties of N_{heg} and R_{mc} are combined. The final results are summarized in Table 7, together with the estimated neutron background from our previous publication [7]. This new evaluation presents a major improvement in the SSNR probability calculation and an *in situ* normalization against the measured HEGs in the data, therefore supersedes the previous.

Table 6 Predicted SSNR and HEG events in counts/day and their ratios in PandaX-II using the new generators.

Components	Run 9			Run 10		
	# SSNR	# HEG	Ratio	# SSNR	# HEG	Ratio
PTFE	1.9×10^{-3}	5.8×10^{-2}	1/30.8	2.0×10^{-3}	5.8×10^{-2}	1/28.8
Cryostat	3.4×10^{-4}	2.8×10^{-3}	1/8.2	3.5×10^{-4}	2.8×10^{-3}	1/7.9
PMT Stem	1.2×10^{-4}	1.3×10^{-3}	1/10.4	1.6×10^{-4}	1.3×10^{-3}	1/7.8
PMT Window	5.1×10^{-6}	3.9×10^{-4}	1/76.3	6.5×10^{-6}	3.9×10^{-4}	1/59.7
Total	2.3×10^{-3}	6.2×10^{-2}	1/26.6	2.6×10^{-3}	6.3×10^{-2}	1/24.6

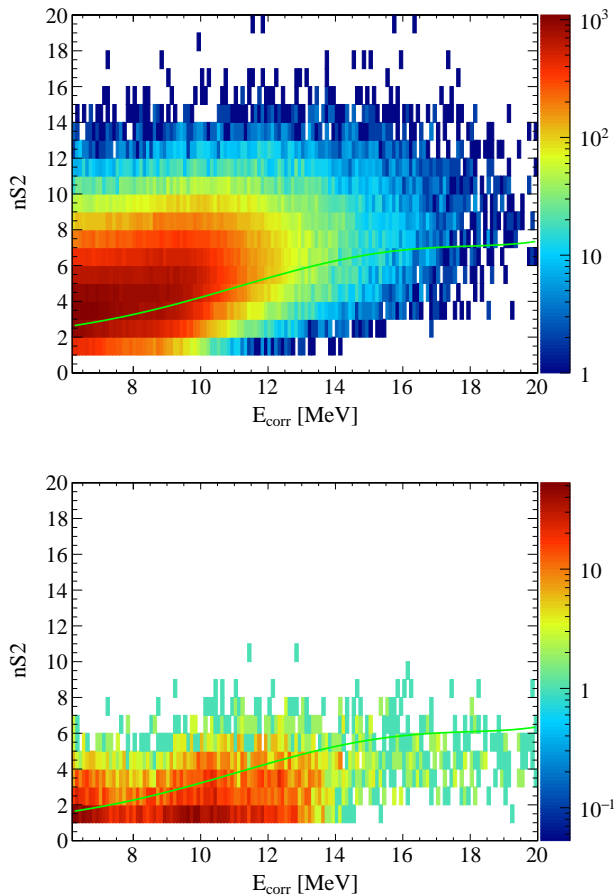
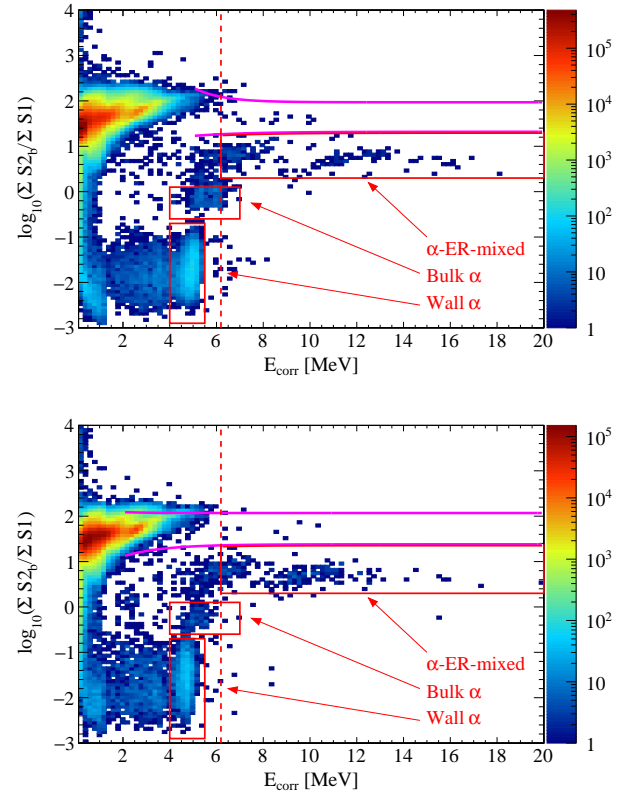
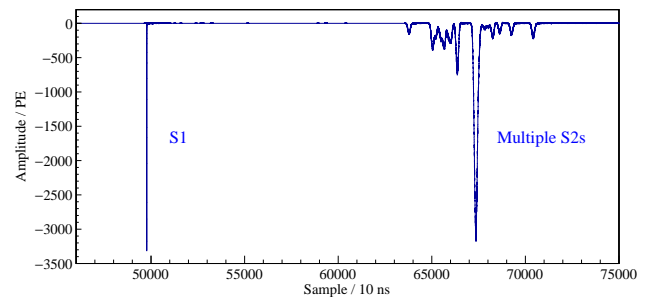
**Figure 7** The distribution of number of S2s vs. E_{corr} for HEGs in AmBe data (top) and high energy α -mixed events in DM data (bottom), Run 9 and Run 10 combined. The green curve represents the α -rejection cut.**Figure 8** The distribution of $\log_{10}(\sum S2_b / \sum S1)$ vs. E_{corr} for events with the α -rejection cut in Run 9 (top) and Run 10 (bottom) DM data.**Figure 9** An example HEG waveform from Run 10 DM data.

Table 7 The neutron background events in Run 9 and Run 10 evaluated with the improved method. The results from our previous publications are shown for comparison.

Methods	Run 9 DM	Run 10 DM
This work	0.66 ± 0.24	0.47 ± 0.25
Ref. [7]	0.85 ± 0.43	0.83 ± 0.42

6 Summary

We performed a detailed study on the neutron background originating from detector materials in the PandaX-II experiment. An improved neutron generator model that incorporates the correlated emission of neutron(s) and γ (s) was developed and benchmarked. A novel data-driven method, with a robust connection between the SSNR and HEG events, was used to predict the neutron background in PandaX-II. The improved neutron background levels are lower than those reported before and are more reliable with well-controlled uncertainties. In the next generation of PandaX-II, i.e., the 4-ton scale PandaX-4T experiment [23], a solid estimation of the neutron background is expected to be achieved by applying this new method. It can be more generally employed in the neutron background evaluation in other dark matter experiments.

This project has been supported by a Double Top-class grant from Shanghai Jiao Tong University, grants from National Science Foundation of China (Nos. 11435008, 11505112, 11525522, 11775141 and 11755001), a grant from the Ministry of Science and Technology of China (No. 2016YFA0400301). We thank the Office of Science and Technology, Shanghai Municipal Government (No. 11DZ2260700, No. 16DZ2260200, No. 18JC1410200) and the Key Laboratory for Particle Physics, Astrophysics and Cosmology, Ministry of Education, for important support. This work is supported in part by the Chinese Academy of Sciences Center for Excellence in Particle Physics (CCEPP) and Hongwen Foundation in Hong Kong. Finally, we thank the CJPL administration and the Yalong River Hydropower Development Company Ltd. for indispensable logistical support and other help.

- 1 Virginia Trimble. Existence and nature of dark matter in the universe. *Annual Review of Astronomy and Astrophysics*, 25(1):425–472, 1987.
- 2 Mark W. Goodman and Edward Witten. Detectability of Certain Dark Matter Candidates. *Phys. Rev.*, D31:3059, 1985. [325(1984)].

- 3 Yu-Cheng Wu et al. Measurement of Cosmic Ray Flux in China Jinping underground Laboratory. *Chin. Phys.*, C37(8):086001, 2013.
- 4 XiGuang Cao et al. PandaX: A Liquid Xenon Dark Matter Experiment at CJPL. *Sci. China Phys. Mech. Astron.*, 57:1476–1494, 2014.
- 5 Andi Tan et al. Dark Matter Results from First 98.7 Days of Data from the PandaX-II Experiment. *Phys. Rev. Lett.*, 117(12):121303, 2016.
- 6 Tao Zhang, Changbo Fu, Xiangdong Ji, Jianglai Liu, Xiang Liu, Xuming Wang, Chunfa Yao, and Xunhua Yuan. Low Background Stainless Steel for the Pressure Vessel in the PandaX-II Dark Matter Experiment. *JINST*, 11(09):T09004, 2016.
- 7 Xiangyi Cui et al. Dark Matter Results From 54-Ton-Day Exposure of PandaX-II Experiment. *Phys. Rev. Lett.*, 119(18):181302, 2017.
- 8 W.B. Wilson et al. SOURCES 4A: A Code for Calculating (α , n), Spontaneous Fission, and Delayed Neutron Sources and Spectra. Technical Report LA-13639-MS, Los Alamos National Laboratory, 1999.
- 9 <http://en.atom-hitech.com/product/51.html>.
- 10 S. Agostinelli et al. GEANT4: A Simulation toolkit. *Nucl. Instrum. Meth.*, A506:250–303, 2003.
- 11 John Allison et al. Geant4 developments and applications. *IEEE Trans. Nucl. Sci.*, 53:270, 2006.
- 12 <https://wwwndc.jaea.go.jp/jendl/jendl.html>.
- 13 Wenqiang Gu. *A study of the Anti-neutrino Flux From the Reaction of the Daya Bay Experiment*. PhD thesis, Shanghai Jiao Tong University, 2018.
- 14 Andi Tan et al. Dark Matter Search Results from the Commissioning Run of PandaX-II. *Phys. Rev.*, D93(12):122009, 2016.
- 15 Brian Lenardo, Kareem Kazkaz, Aaron Manalaysay, Jeremy Mock, Matthew Szydagis, and Mani Tripathi. A Global Analysis of Light and Charge Yields in Liquid Xenon. *IEEE Trans. Nucl. Sci.*, 62(6):3387–3396, 2015.
- 16 Xuming Wang, Xun Chen, Changbo Fu, Xiangdong Ji, Xiang Liu, Yajun Mao, Hongwei Wang, Siguang Wang, Pengwei Xie, and Tao Zhang. Material Screening with HPGe Counting Station for PandaX Experiment. *JINST*, 11(12):T12002, 2016.
- 17 E. Aprile et al. Physics reach of the XENON1T dark matter experiment. *JCAP*, 1604(04):027, 2016.
- 18 <http://cern.ch/geant4-userdoc/UsersGuides/PhysicsReferenceManual/BackupVersions/V10.3/fo/PhysicsReferenceManual.pdf>.
- 19 Qihong Wang et al. in preparation. 2019.
- 20 Jerome Verbeke, Chris Hagmann, and Doug Wright. Simulation of Neutron and Gamma Ray Emission from Fission and Photofission. LLNL Fission Library 2.0.2. Technical Report UCRL-AR-228518-REV-1, Lawrence Livermore National Laboratory, 2016.
- 21 https://nuclear.llnl.gov/simulation/fission_v2.0.2/fission_v2.0.2.tar.gz.
- 22 J.M. Verbeke, J. Randrup, and R. Vogt. Fission Reaction Event Yield Algorithm FREYA 2.0.2 User Manual. Technical Report LLNL-SM-705798, Lawrence Livermore National Laboratory, 2017.
- 23 Hongguang Zhang et al. Dark matter direct search sensitivity of the PandaX-4T experiment. *Sci. China Phys. Mech. Astron.*, 62(3):31011, 2019.